Accepted Manuscript

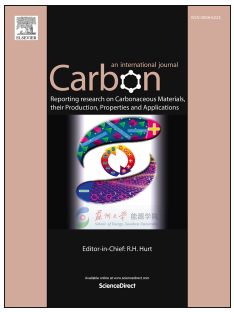

Graphene surface structure in aqueous media: Evidence for an air-bubble layer and ion adsorption

Liangzhi Zhou, Luisa Islas, Nicholas Taylor, Oier Bikondoa, Eric Robles, Wuge H. Briscoe

PII: S0008-6223(18)31012-1

DOI: https://doi.org/10.1016/j.carbon.2018.10.093

Reference: CARBON 13611

To appear in: *Carbon*

Received Date: 13 August 2018

Revised Date: 14 October 2018

Accepted Date: 30 October 2018

Please cite this article as: L. Zhou, L. Islas, N. Taylor, O. Bikondoa, E. Robles, W.H. Briscoe, Graphene surface structure in aqueous media: Evidence for an air-bubble layer and ion adsorption, *Carbon* (2018), doi: https://doi.org/10.1016/j.carbon.2018.10.093.

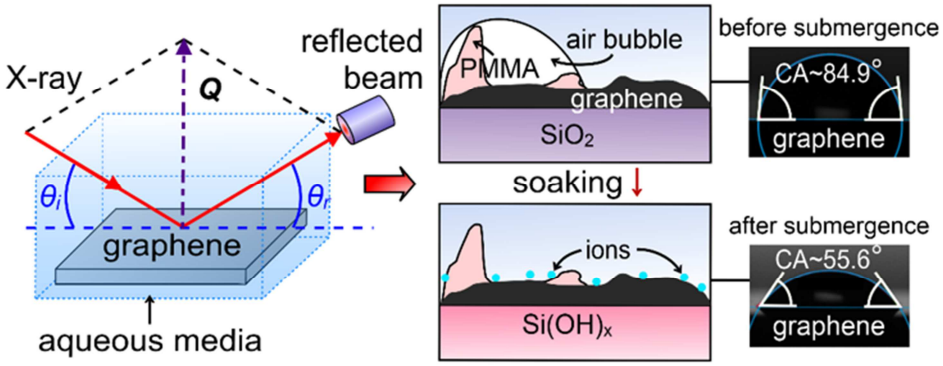

Graphene surface structure in aqueous media: Evidence for an air-bubble layer and ion adsorption

Liangzhi Zhou[1], Luisa Islas [1], Nicholas Taylor[1], Oier Bikondoa[2,3], Eric Robles[4], and Wuge H. Briscoe[1]*

[1]School of Chemistry, University of Bristol, Cantock's Close, Bristol BS8 1TS, UK

[2]XMaS, the UK-CRG, European Synchrotron Radiation Facility (ESRF), 6 Rue Jules Horowitz, BP 220, 38043 Grenoble CEDEX 9, France

[3]Department of Physics, University of Warwick, Gibbet Hill Road, Coventry CV4 7AL, UK

[4]Household Care Analytical, Procter & Gamble Newcastle Innovation Centre Whitley Road, Longbenton, Newcastle NE12 9TS, UK

Abstract: Understanding graphene surface structure in aqueous media is essential for its biotechnological applications. Here, using synchrotron X-ray reflectivity (energy 14 keV), AFM imaging, and contact angle measurements, we have investigated the surface structure of CVD graphene on SiO_2/Si in water and phosphate buffered saline (PBS) at 25-60 ºC. We found a diffuse layer immediately adjacent to graphene with a scattering length density (SLD) of 6.72×10^{-6} Å^{-2}, attributed to the presence of air bubbles on graphene under water. AFM imaging was indicative of interfacial inhomogeneity, but did not provide conclusive topography information on the bubble-covered graphene-water interface. The diffuse layer diminished after the graphene was submerged in water for 24 h at 25 ºC. This is also evident from its enhanced wettability, with the water contact angle on graphene decreasing from 84.9±0.4° to 55.6±0.4° after submergence. An additional layer atop graphene appeared after soaking, with a thickness 10.1 Å, and a higher SLD of 19.5×10^{-6} Å^{-2} at 25 ºC, which increased to 11.8 Å and 21.8×10^{-6} Å^{-2} at 60 ºC in PBS, respectively. We discuss this observation in terms of ion mobility, possible formation of a silanol layer on the SiO_2 substrate, and water structure disruption at higher temperatures.

1 Introduction

Since the first exfoliation of graphene [1, 2], it has attracted intense interest in both scientific research and industrial applications as a promising 2D material due to its physicochemical

* Corresponding author. Tel: +44 (0)117 3318256. E-mail: wuge.briscoe@bristol.ac.uk (Wuge Briscoe)

properties [2, 3], including electronic properties [4], high thermal conductivity [5], mechanical strength [6], optical transparency [7], and large surface area to volume ratio. For instance, numerous studies have explored the high electrical conductivity and carrier mobility of graphene at room temperature (RT) [2] for usage in energy storage devices [8, 9] and transistors [10, 11]. With a large active surface area, one-atom thickness, and delocalised π electrons, graphene enables the detection of changes in the surrounding environment with molecular level sensitivity [12], *e.g.* for sensing gases [12], humidity [13], and biomolecules [14]. Potential bioanalytic applications of graphene have also attracted wide attention. For these applications, graphene often needs to be exposed to or in contact with aqueous systems. Therefore, it is important to understand the structure of graphene in water, since the physical properties of graphene are influenced by its structure (*i.e.* thickness [15, 16], lattice order [17, 18], defects [19, 20], and impurities [21]) and that of the underlying substrate [22].

Several investigations have been reported on the effects of water on graphene and its derivatives. Using contact angle (CA) measurements, it has been shown that the structure (such as thickness and layer stacking) and charge transfer between graphene and its surrounding environment could influence the interaction between water and graphene [13], although the mechanism remains unclear. Specifically, it has been reported that the hydrophobicity of graphene on a copper foil [13] and a SiC wafer [23] increased with the number of graphene layers. Molecular dynamic simulations showed that free-standing graphene was hydrophobic [23, 24], due to the hydrogen bond network within a water double layer formed on the graphene surface.

Studies on the interaction between biomolecules and graphene and its derivatives in aqueous media have also been reported [14, 25]. A number of techniques for studying interfacial adsorption, such as atomic force microscopy (AFM) [26, 27], imaging total internal reflection fluorescence correlation spectroscopy (ITIR-FCS) [27], quartz crystal microbalance with dissipation monitoring technique (QCM-D), and dual polarization interferometry (DPI) [28], have been applied to graphene. In addition, adsorption of biomolecules on graphene can be monitored by changes in the electrochemical performances of graphene, using techniques such as cyclic voltammetry and differential pulse voltammetry [29, 30].

However, these methods provide limited structural information on the adsorbed molecular layer at the buried graphene-water interface. X-Ray reflectivity (XRR) is a rigorous and quantitative technique for probing structural features of nanofilms at buried interfaces [31-35]

with sub-Ångström resolution. It has been used to study epitaxial graphene on SiC in air [36, 37] and in water [23]. Moreover, in combination with photoemission electron microscopy (PEEM) and AFM imaging, XRR has been recently used to provide detailed structural information such as the layer thickness, coverage, morphology, and composition of chemical vapor deposited (CVD) graphene on Si/SiO_2 substrates, where a slight thermal expansion of graphene has also been observed upon heating it from 25 °C to 60 °C [38].

Here, we have used synchrotron XRR to investigate the graphene-water interface at different temperatures (25-60 °C), complemented by AFM imaging and contact angle measurements at RT. In addition, the effect of phosphate buffered saline (PBS) on the graphene surface structure has also been probed. This was motivated by a previous report that soaking graphene in water for 24 h facilitated lipid *bilayer* formation in PBS solutions [39], instead of *monolayers* without soaking [40]. In this work, the structure of graphene was studied by XRR before and after submergence in Milli-Q® water for 24 h. Our results provide valuable information on the structure of the graphene-water interface and the interaction between the ions and graphene in an aqueous medium. The study also demonstrates the feasibility of XRR to study the adsorption of ionic and molecular species and their thin film structure on the graphene surface, and such fundamental knowledge underpins bioanalytic applications in which graphene comes into contact with liquids.

2 Experimental methods

2.1 Materials

CVD graphene used in this study was purchased from *Graphenea Inc*[1]. Graphene was grown on a copper (Cu) foil and then covered with a spin-cast polymethylmethacrylate (PMMA) layer. The Cu foil was then etched away using $FeCl_3$ and the graphene with PMMA transferred onto a 1 cm × 1 cm Si wafer with a 300 nm SiO_2 oxide layer. Finally, the PMMA layer was washed off using organic solvents. Our recent XPS analysis of the graphene samples obtained from the same supplier indicated the presence of PMMA residues, whilst no Cu (the CVD substrate) and $FeCl_3$ (the etchant) was detected on the samples [38], an observation consistent with literature [21]; and the XRR analysis indicated that the graphene samples studied possessed a thickness of 13.0±1.0 Å [38]. Ultrapure Milli-Q® water with resistivity of 18.2 MΩ cm and a total organic content (ToC) of 3-4 ppb at 25 ºC and 0.01 M

[1] https://eu.graphenea.com/

PBS (0.0027 M KCl and 0.137 M NaCl, pH = 7.4, at 25 °C, Sigma-Aldrich®) were used for solution preparation.

2.2 Experimental methods

The AFM measurements were conducted by PeakForce feedback control (Bruker, CA, USA) in air and aqueous systems using a MultiMode VIII microscope with a NanoScope V controller. The cantilever employed was SCANASYST_FLUID+ with nominal spring constant of 0.7 N m^{-1} and a tip radius of 2 nm. The static contact angle measurements were performed using the Sessile drop method on a KRÜSS® DSA100 instrument. Synchrotron XRR measurements were performed at beamline BM28-XMaS, European Synchrotron Radiation Facility (ESRF), Grenoble, France. A custom-designed liquid cell shown schematically in Figure 1 [32, 38, 41] was used for XRR experiments, with graphene samples mounted on the sample stage. The cell was sealed by two polyester (Mylar®) windows, providing a total liquid capacity of 5 ml.

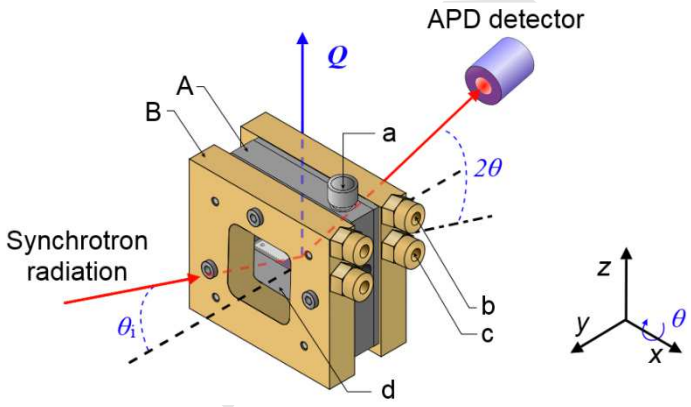

Figure 1. Schematic of the XRR experiment setup with an incident synchrotron X-ray beam reflected from the sample with an incident angle θ_i to the avalanche photodiode detector (APD) that collects the specular reflection. The momentum transfer is defined as $\boldsymbol{Q} = 4\pi sin(2\theta/2)/\lambda$, where λ is the wavelength of the X-ray beam. The sample of 1 cm × 1 cm in size is clamped onto a stainless-steel stage (d) in a customised liquid cell (A) with a nozzle (a) that allows in situ liquid/gas exchange. Temperature control can be provided by two heating jackets (B), which can be connected to a water circulating bath *via* an inlet (c) and an outlet (b).

To investigate the influence of submerging graphene in water on its surface structure, XRR curves were collected on graphene within 10 min after it was exposed to Milli-Q water, which was the time required for sample alignment. The graphene then remained submerged

under water for a further 23-24 h before XRR measurements were made again. Subsequently, water was replaced by PBS, and the XRR curves were collected at 25 °C, 40 °C and 60 °C, after which the samples were cooled back to 25°C to compare with the initial stage. As a control, bare graphene that had not been submerged in water was also measured in PBS at RT. Each heating and cooling step took ~10 min and ~20 min, respectively, with a furhter10 min allowed for thermal equilibrium before the measurement was made.

The X-ray beam energy was 14 keV (with a corresponding wavelength λ = 0.8856 Å), and the beam size as defined by aperture slits was 100 μm (vertical FWHM) × ~255 μm (horizontal FWHM). A consideration for XRR measurements in aqueous media is the absorption of X-rays by water. The liquid thickness in the custom-designed XRR cell (*cf.* Figure 1) was 1 cm, permitting ~20% transmission at 14 keV X-ray energy, which is sufficient for XRR measurements [41]. Specular XRR scans were collected with the incident angle θ_i varying from 0.06-3.0º and the reflection angle $\theta_r = \theta_i$, corresponding to a momentum of transfer $\boldsymbol{Q} = 4\pi\sin(2\theta/2)/\lambda$ range of 0.015-0.74 $Å^{-1}$, where $2\theta = \theta_r + \theta_i$. The specular reflection was detected at each angle using an avalanche photodiode detector (APD), as shown in Figure 1. XRR data fitting was performed by using *Motofit* in Igor Pro (WaveMetrics, Inc., Lake Oswego, OR, USA), using the Abeles matrix method, which generates the same result as Parratt's recursive method [42]. A genetic algorithm optimisation is adopted in this software to minimize the χ^2 value, which shows the goodness of fitting,

$$\chi^2 = \sum_{n=1}^{L} \frac{1}{L-P}\left(y_{0,n} - y_n\right)^2, \qquad \text{Equation 1}$$

where L is the number of collected data points; P the number of variables which are varied during fitting, *e.g.* the number of layers (n), the scattering length density (SLD, ρ_n, definition and calculation in Supporting Information section SI-1), the thickness (t_n), and the interfacial roughness ($R_{a,n}$); y_0 the measured value; and y the corresponding theoretically fitted value yielded from the used parameters. Reflectivity curves with mild fringes (*i.e.* reflectivity R variations w.r.t. $\boldsymbol{Q}$) were plotted as $R\boldsymbol{Q}^4$ *vs.* $\boldsymbol{Q}$ instead of log$R$ *vs.* $\boldsymbol{Q}$, as shown in Figure 2b and Figure 5a, to show more clearly the Kiessig fringes [43]. In total, 12 XRR measurements on 3 graphene samples were studied in 2 separate synchrotron experiments, and the results shown below are representative of these measurements. The XRR curves collected from different graphene samples were reproducible.

3 Results and discussion

3.1 XRR of the graphene-water interface

XRR data fitting used a Slab Model, with ρ_n, t_n, and $R_{a,n}$ the SLD, thickness, and roughness of the n^{th} slab/layer as defined in

Figure 2a. This yielded fits (χ^2 <0.0012) for the reflectivity curves of the graphene samples in different conditions. Figure 2b shows example XRR curves for bare graphene in air (circles) and water (triangles), and the soaked graphene in water (squares), with the fitted reflectivity curves shown as continuous lines. The XRR intensity oscillations (Kiessig fringes [44]) damped (*i.e.* became less pronounced) in water compared to air due to reduced SLD contrast with graphene.

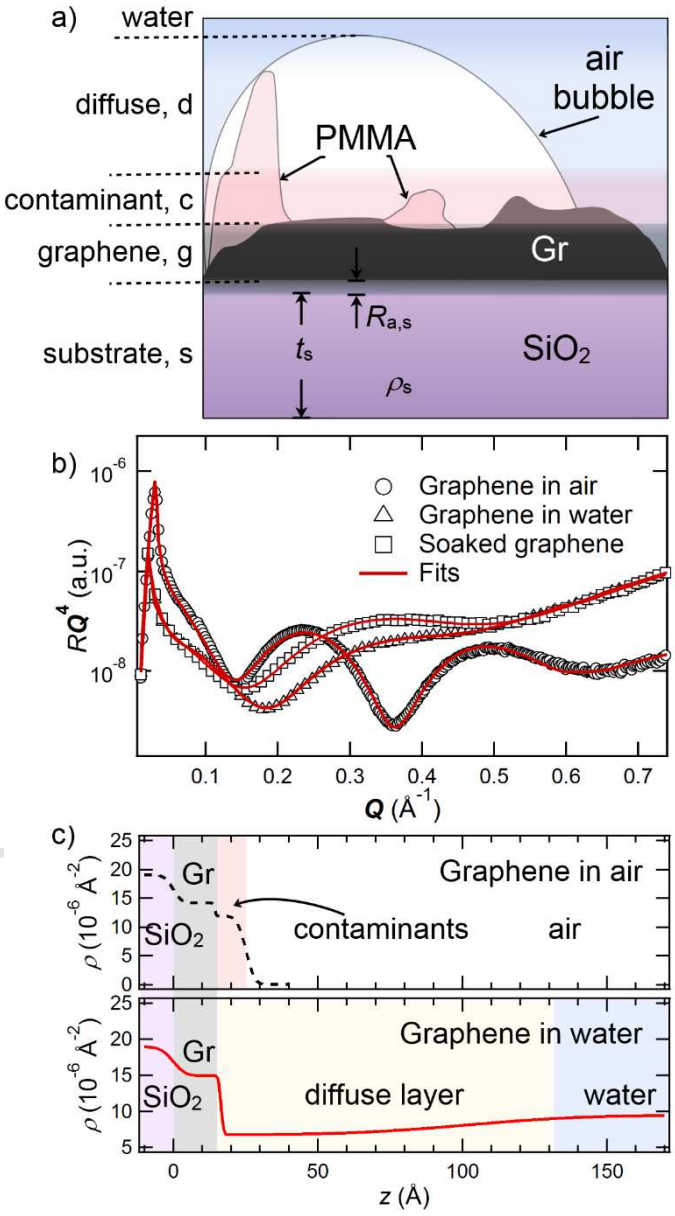

Figure 2. a) Physical model used to fit the XRR curves of graphene in water. b) The experimental (open symbols) and fitted (solid lines) XRR curves plotted as RQ^4 vs. Q for graphene in air (circles), in water (triangles), and 24 h-water soaked graphene (squares). The fitting parameters are listed in Table S2 in SI-1). c) The fitted SLD ρ_n of the graphene sample in air (dash line) and in water (solid line), plotted against z, the distance form the SiO_2 surface, with the SLD variations highlighted in different coloured regions across the interfaces of the graphene sample in air and in water. Each coloured region, with the width representing t_n, represents a modelled layer as defined in a). The contaminant layer on graphene (represented as **Gr**) in air [38] is highlighted in pink, and a diffuse layer is present on the graphene in water.

From the fitted SLD profile of graphene in air shown in
Figure 2c, the interfacial structure of the sample consisted of a graphene layer (represented as **Gr** in
Figure 2a) with a contaminant layer comprising graphene multilayers and PMMA residues atop. The latter layer exhibited a thickness t_c = 11.8±1.2 Å and an SLD $\rho_c = 9.80\times10^{-6}$ Å^{-2} [38]. After the injection of water or PBS in the XRR liquid cell (*cf.* Figure 1), the contaminant layer on the graphene sample seemed undetectable, substituted by a diffuse layer at the interface with an SLD profile which gradually increased from ρ_d = ~6.7×10^{-6} Å^{-2} to $\rho_{water} = 9.44\times10^{-6}$ Å^{-2} of the bulk water. The SLD of this diffuse layer was smaller than that of graphene ($\rho_g = 18.20\times10^{-6}$ Å^{-2}) or PMMA ($\rho_{PMMA} = 10.81\times10^{-6}$ Å^{-2}), and was between that of air (ρ_{air} = 0 Å^{-2}) and water, whilst the high roughness $R_{a,d}$ (>30 Å) value indicates a highly heterogenous interfacial structure (fitted values shown in Table 1). We suggest that this reduced SLD of the interfacial layer could be attributed to the formation of flattened air bubbles of nonuniform coverage on the graphene surface, as shown schematically in
Figure 2a. The mixed SLD (ρ_{mix}) of a binary mixture could be calculated as

$$\rho_{mix} = \phi\rho_1 + (1-\phi)\rho_2, \qquad \text{Equation 2}$$

where ϕ is the volume fraction of one component and ρ_i is the SLD of constituent i, respectively; the volume fraction of air in this diffuse layer, ϕ_{air}, can be then calculated, which is ~30 % as shown in Table 1 and the calculation method of ϕ_{air} is described in detail in SI-1.3. Such an SLD reduction has been previously observed on a rough polystyrene surface

[45]. Further AFM imaging suggested that this diffuse layer was a consequence of both the contaminant and the air bubbles present on the surface [46].

Table 1. Fitting parameters for the XRR data collected from graphene in air, in water, in PBS, and 24 h water-soaked graphene in water at 25 ºC.

Sample	**Layers in the Slab Model**	t_n **(Å)**	ρ_n **(10^{-6} Å^{-2})**	$R_{a,n}$ **(Å)**	ϕ_{air} **(%)**	χ^2 **(10^{-3})**
Graphene in air at 25ºC	Contaminants	10.8	11.87	2.4	100	1.11
	Graphene	14.4	14.13	0.4		
	SiO_2	3000	19.01	2.4		
Graphene in water at 25ºC	Diffuse layer	84.9	6.72	31.9	36.7	0.47
	Graphene	16.5	14.93	0.7		
	SiO_2	3000	18.91	3.4		
Graphene in PBS at 25 ºC	Diffuse layer	118.3	6.75	49.3	30.9	0.71
	Graphene	15.4	19.71	4.5		
	SiO_2	3000	18.91	3.5		
Soaked graphene in water at 25ºC	Ion adsorbed layer	10.1	19.45	1.0	0	0.19
	Graphene	5.0	14.91	2.3		
	silanol	78.9	21.32	4.6		
	SiO_2	3000	18.96	69.7		

3.2 AFM imaging at the graphene-water interface

AFM topological images (Figure 3a) have also been collected to reveal the morphology of the graphene-water interface and were processed using the *NanoScope Analysis* software. We have previously studied the ~~The~~ topological images of the graphene sample in air, which indicated that the surface was comprised of the SiO_2 substrate, graphene, and the defects (highlighted in white rectangles in Figure 3a) that consisted of PMMA and multilayer graphene flakes [38]. However, it was a lot more challenging to obtain good quality, reproducible images under water, which is probably ascribable to a more complicated structure with inhomogeneous coverage. In addition, the presence of soft air bubbles could make it difficult for the AFM scanning tip to engage with surface. As a result, the AFM images of the graphene-water interface did not provide conclusive supporting evidence for the presence of the bubbles.

For the example under-water image shown in Figure 3a, the maximum difference in the height, Δh_{max}, increased by ~11 Å compared to air (

Table 2). Meanwhile, the graphene roughness given by the height deviation R_{ave} and height root-mean square R_{sq} also increased, consistent with a more inhomogeneous interface caused by the formation of air bubbles (high resolution AFM topological images in Figure S3a in SI-2).

Table 2. The maximum difference in the relative height, Δh_{max}, the root-mean square average, R_{sq}, and the arithmetic average values of height deviations, R_{ave}, of the surface height deviations in the AFM topological images of graphene in air and in water following the plane fitting.

	Δh_{max} (Å)	R_{sq} (Å)	R_{ave} (Å)
In air	124	6.61	4.68
In water	135	10.8	8.37

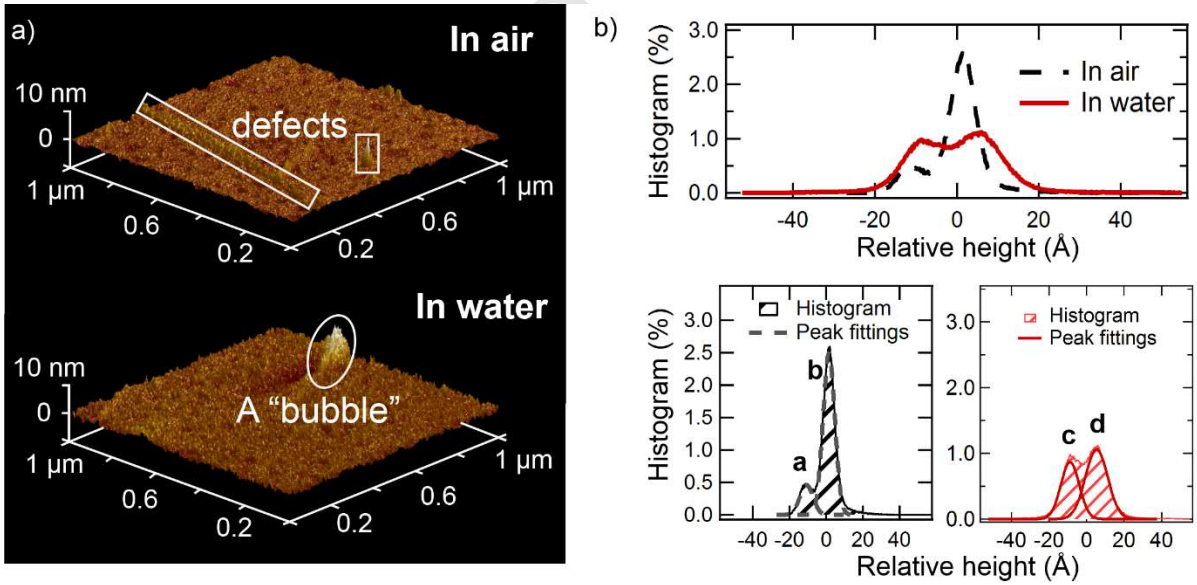

Figure 3. a) Example AFM topological images of graphene and its defects (indicated by the rectangles) in air, and a possible bubble (indicated by an oval) in water on a 1 μm × 1 μm scale; and b) the corresponding histograms of height distributions on the sample surface with the Gaussian peak fittings for the measurements in air (left) and in water (right).

It can be observed from the Gaussian peak fittings shown in Figure 3b that the height distribution on the solid-water interface (with FWHM values of peaks **c** and **d** 11.5 Å and 10.6 Å, respectively) was broader than that at the air-water interface (with peaks **a** and **b** possessing FWHM values 8.4 Å and 7.5 Å, respectively), suggesting the existence of more inhomogeneous structures on the graphene-water interface compared to air. Particularly, as indicated by an oval in Figure 3a, a bubble-like area of size ~189 nm (length) × 88 nm (width) × 10 nm (height) was detected. The air bubble layer from XRR fitting (*cf.* Table 1) has a smaller thickness (t_d = 84.9 Å) but a higher roughness ($R_{a,d}$ = 31.9 Å). One possible reason for the differences is that the XRR measures and thus gives the average value of a surface layer over a much larger footprint (~200 µm × 1 cm), whilst AFM measures a much smaller sample area (~ a few μm^2) and thus reflects a much more localized structure [38]. It should be borne in mind that a more complex structure could be present on graphene, including residual PMMA contaminants ~~and~~, graphene multilayers, and the potential contaminants accidentally introduced during the experiments [47], which could not be distinguished by topological images only. Although AFM imaging did not provide conclusive topography information on graphene under water, it indicated that the interfacial structure was different from that in air. It was also qualitatively consistent with the XRR results which were indicative of an inhomogeneous interface. Further effort with AFM imaging remains a focus of our future work.

3.3 Effect of submerging CVD graphene on Si/SiO_2 under water

The sessile drop water contact angles (CAs) of graphene before and after soaking graphene in water for 24 h are shown in Figure 4b. For the soaked graphene samples, the water residues were removed by two methods: drying naturally or using an Ar flow to dry the surface gently. A noticeable reduction of graphene water CA was observed with both methods. The results (described in detail in SI-3) showed that the water CA on graphene decreased from 84.9±0.4° to 55.6±0.4° after it had been submerged under water for 24 h, indicating that the graphene sample became more hydrophilic. It has been shown that prolonged exposure to water could lead to graphene detachment from the substrate [50]. However, our XRR analysis (see below) shows unequivocally the presence of graphene after water soaking in our case. Whether graphene is hydrophobic or hydrophilic is still somewhat controversial in the literature. Graphene was once believed to have similar wettability to graphite (water CA = ~80-100°), while some CA measurements suggested it was hydrophobic, and even superhydrophobic [48]. More recent studies showed that the interaction between water and graphene was

affected by the graphene surface structure and related parameters, such as the graphene layer thickness [23, 49], the presence of defects [23, 48] and adsorbates [24, 48], underlying substrates [50], and the doping of graphene [51]. Both the surface energy and the topological features should contribute to the observed wettability of such a heterogeneous material. Thus, it is possible that graphene hydrophobicity reflects its various surface roughness and related chemical inhomogeneities due to different fabrication methods [48, 49].

It has been reported that trapped air bubbles could form at the solid-liquid interface particularly when nanotextures or multi-scale roughness were present at the interface, resulting in the Cassie–Baxter wetting state, which would then lower the solid-liquid adhesion and manifest in apparent higher hydrophobicity [52, 53]. If water permeates the surface textures, transforming the wettability from the Cassie-Baxter state to the Wenzel state [54], the hydrophobicity of the material would decrease, consistent with our observation of the decreased CA after 24 h water submergence. In addition, the SLD profile in Figure 4a indicates that no diffuse air-bubble layer was present on top of graphene after water-soaking, and that water had fully spread on the surface, as shown schematically in Figure 4c. The fitted graphene thickness $t_{g(water)}$ = 5.0 Å with $\rho_g = 14.91\times10^{-6}$ Å^{-2}, decreased appreciably after soaking, compared with the graphene thickness $t_{g(air)}$ = 14.4 Å detected in air. In the meantime, an additional layer appeared, with a higher SLD $\rho_a = 19.5\times10^{-6}$ Å^{-2}, and thickness t_a = 10.1 Å. The total thickness $t_{total} = t_{g(water)} + t_a$ = 15.1 Å is very similar to $t_{g(air)}$, and we attributed this observation to the adsorption of ions within the defect structures on graphene, which will be discussed below in section 3.4.

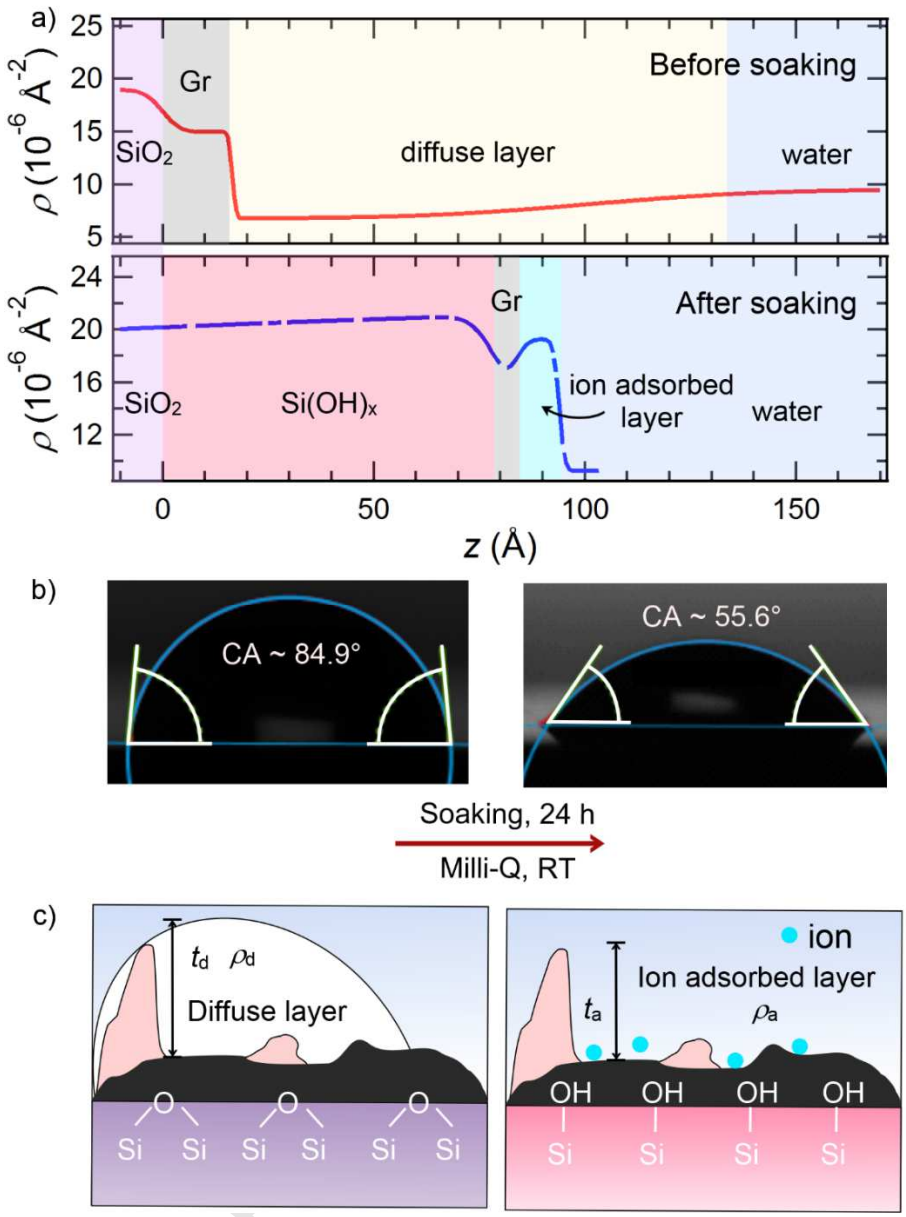

Figure 4. a) Fitted XRR SLD profiles in water of the un-soaked graphene (red solid line) and soaked graphene (blue dashed line), with the coloured regions representing different layers in the Slab Model used to fit the data. b) The water CA = 84.9º of a bare graphene sample reduced to CA = 55.6º after soaking in Milli-Q for 24 h. The diminishing of the air bubble layer, the hydration of the SiO_2 substrate, and the formation of the ion adsorbed layer upon soaking are schematically illustrated in (c).

Furthermore, the SLD of the underlying substrate increased from $\rho_s = 18.91\times10^{-6}$ Å^{-2} before water soaking, a value matching the theoretical SLD of SiO_2, to $\rho_s = 21.32\times10^{-6}$ Å^{-2} after soaking (*cf.*

Table 2). We attributed this to the formation of $Si(OH)_x$ by the rehydration of the amorphous silica, as the SLD of silanol is ρ = 28.72×10^{-6}. Water molecules can permeate through graphene lattices and interact with silica substrate [55], leading to a higher electron density due to the formation of hydroxyl groups on the surface. The silica substrate is normally stable in water, and the formation of silanol layer is not considered in most of the cases, because of the low diffusion velocity of water molecules (only 6 Å per 1000 min at 25 ºC) in bulk silica. However, molecular diffusion can be accelerated by increasing temperature [56]. We thus postulate that the prolonged submergence of the sample in water and subsequent increased temperature during XRR measurements led to the formation of detectable silanol groups, which could also contribute to the enhanced wettability observed after water soaking.

The fitted thickness of the silanol layer is t_s = ~75 Å, a value much higher than the theoretical one (8.64 Å after soaking in water for 24 h [56]), and the ρ_s profile also decreased gradually towards the bulk silica. Meanwhile, the fitted roughness of the silica substrate is also high $R_{a,silica}$ = ~65 Å. It is possible for water to penetrate the amorphous silica, leading to a relatively thick and rough interfacial layer. The observation of this silanol layer underneath graphene has important implications, as the acidity of silanol could lead to high affinity for ions and biomolecules [57]. It has also been reported that the presence of silanol on the SiO_2 substrate underlying graphene could change the electric properties of graphene, due to the electric dipoles possessed by the adsorbed water [58]. This could enhance the doping of graphene to water, thus enhancing its wettability.

3.4 Effect of temperature and PBS on CVD graphene on Si/SiO_2

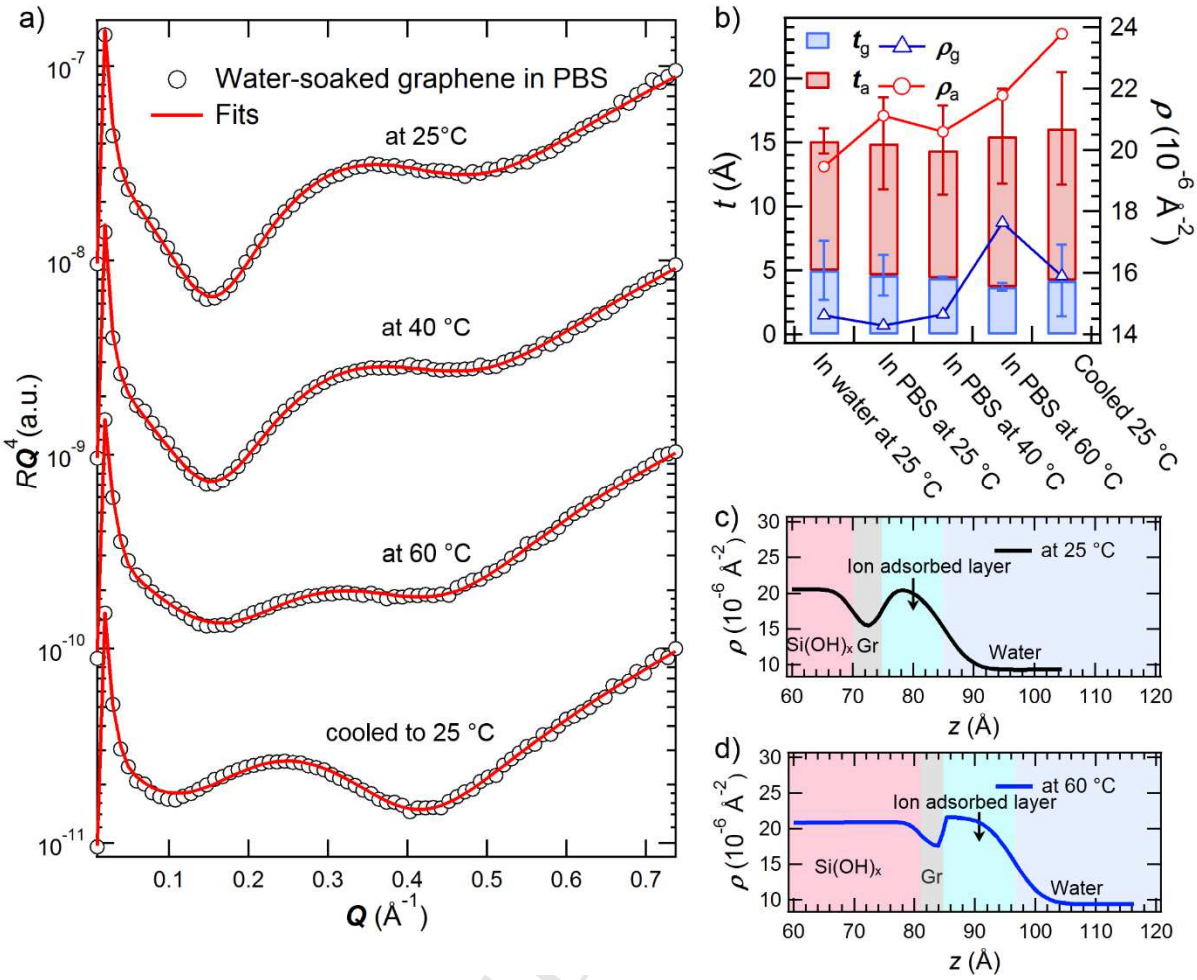

Figure 5. a) The experimental (open circles) and fitted (solid lines) XRR curves (offset vertically for clarity) of water-soaked graphene in PBS at different temperatures, with the fitting parameters (t_n, ρ_n and $R_{a,n}$) tabulated in Table S2. The fits show that the graphene thickness t_g remained at ~4.2 Å at all temperatures; while its SLD was relatively constant at ρ_g ~15×10^{-6} Å^{-2} at lower temperatures, it increased to ρ_g = 17.6×10^{-6} Å^{-2} at 60 °C. Similarly, the SLD and thickness of the ion adsorbed layer ρ_a and t_a increased at 60 °C, and the increment remained after cooling back to RT as shown in b). The SLD profiles of graphene samples at 25 °C and 60 °C are shown in (c) and (d), respectively, which show that the thickness of the silanol layer also increased at 60 °C, with the interface between graphene and the ion adsorbed layer becoming smoother.

Figure 5a shows XRR curves of water-soaked graphene in PBS, at 25 °C, 40 °C, 60 °C, and then cooled back down to 25 °C. The change in the Kiessig fringes is noticeable upon heating and cooling, and the XRR profiles are also different from those in pure water (*cf.*

Figure 2c). The fitting parameters and SLD profiles for these XRR curves are given in Table S2 and Figure S2, respectively, in SI-1. The thickness t_a and SLD ρ_a of the ion adsorbed layer atop graphene (as illustrated in Figure 4c in section 3.3) increased after water was replaced with PBS at RT. In addition, as listed in Table 1, the fitted SLD value $\rho_g = 19.17\times10^{-6}$ Å^{-2} of un-soaked graphene is also higher in PBS than that in air ($\rho_g = 14.93\times10^{-6}$ Å^{-2}). This again is consistent with the assumption of ion adsorption on graphene. It has been shown by molecular dynamics simulations that graphene could attract, due to π-conjunction and polarizability, both cations [59-61] and anions [62, 63], such as Na^+ ($\rho = 86.75\times10^{-6}$ Å^{-2}) and K^+ ($\rho = 55.06\times10^{-6}$ Å^{-2}) in PBS to the graphene-water interface. Furthermore, the fitted SLD profiles to the XRR curves of the soaked graphene in PBS at 25 °C (Figure 5c) and 60 °C (Figure 5d) also show that ion adsorption was promoted upon heating. The thickness and SLD of the ion adsorbed layer increased to t_a = 11.8 Å, and $\rho_a = 21.8\times10^{-6}$ Å^{-2} , with respective increment $\Delta\rho_a = 0.7\times10^{-6}$ Å^{-2} and Δt_a = 1.5 Å compared with 25 °C), whilst the graphene thickness t_g = 4.2 Å (*cf.* the theoretical thickness of a monolayer graphene of 3.35 Å) remained constant, with the fitted SLD in PBS $\rho_g = \sim15\times10^{-6}$ Å^{-2} also comparable to that in air.

The interfacial roughness $R_{a,g}$ between graphene and the ion adsorbed layer decreased at higher temperatures (Figure 5b), which could be due to the ions residing in the defects and on the contaminants of the graphene surface and reducing the apparent roughness. The thickness t_s of the silanol layer also increased upon heating (Figure 5d), thereby promoting ion adsorption to the substrate [57]. The effect of temperature on the ion adsorption can be triggered by the enhanced mobility of ions at higher temperatures [64]. In addition, the structure of graphene itself can also play an important role in response to the temperature-dependent ion adsorption. A simulation study has reported that water could form an ice-like double layer structure on free standing graphene, preventing the interaction between graphene and the bulk solution [24]. This interfacial water structure was found disrupted at 340 K (67 °C), which is close to where we observed enhanced ion adsorption.

4 Summary and concluding remarks

In this study, we have applied synchrotron XRR to characterise the surface structure of graphene in water and PBS. The surface structure of graphene submerged under water for 24 h was also studied. AFM imaging provided inconclusive topological morphology of graphene under water, due to the intrinsic experimental difficulties associated with the technique while

imaging a soft, bubble-covered surface. The surface roughness data however was consistent with a much more inhomogeneous graphene-water interface compared to air. Fitting the SLD to the XRR curves on graphene indicated the presence of an air bubble layer (ρ_d = 6.72×10^{-6} Å^{-2}, t_d = 84.9 Å, and $R_{a,d}$ = 31.9 Å) on top of graphene when firstly immersing it in water. AFM imaging also revealed the presence of isolated bubbles (*e.g.* ~189 nm (length) × 88 nm (width) × 10 nm (height)) on graphene. These bubbles of a few nm in height with a flattened morphology diminished after the graphene sample was submerged under water for a prolonged period. Concurrently, the water contact angle on graphene decreased from 84.9±0.4° (before soaking) to 55.6±0.4° (after soaking), indicating a decrease in its hydrophobicity. This alone is not the sufficient evidence for the diminishment of the air bubble layer, but is consistent with the XRR analysis that indicates such a diminishment. XRR results also suggested that, after water soaking, and the formation of a silanol layer formed on the SiO_2/Si substrate, which could also alter the electric properties of the graphene/silica sample [58] and contribute to the observed reduction in the water contact angle. Furthermore, ion adsorption was inferred from the increased SLD of the layer atop graphene observed on water-soaked graphene in PBS, with the fitted interfacial structure consisting of an additional ion adsorbed layer. The ion adsorption was enhanced by heating the solution to 60 ºC, which was retained after cooling. We attributed this change to the higher ion mobility, the higher ion affinity of the formed silanol layer on the substrate, and the disruption of the ordered water structure at high temperatures as reported previously [24]. These unprecedented results are relevant to bioanalytic and nanotechnological applications of graphene in which its structure at the interface between water and electrolyte solutions is an important consideration to the efficacy and functionality of the devices or the processes. The capability of XRR to detect the air bubbles exist on the hydrophobic interfaces can be also utilized on examining the wettability of a surface with sub-micro precision, compared with CA measurements that only provide the bulk wetting. It will be useful and interesting to further investigate, using the XRR method reported here, graphene samples without the PMMA-residues, to ascertain their effect on the presence of the air bubble layer, the diffuse layer, and ion adsorption. This remains a focus of our future studies.

Acknowledgement

We acknowledge funding from the Engineering and Physical Science Research Council (EPSRC EP/H034862/1, EP/K035746/1 for PeakForce atomic force microscopy that was carried out by Dr R. Harniman in the Chemical Imaging Facility, University of Bristol).

Funding from the Royal Society, the European Cooperation in Science and Technology (CMST COST) Action CM1101, the Consejo Nacional de Ciencia y Tecnologia (CONACyT) Postdoctoral Fellowship 291231, and the Marie Curie Initial Training Network (MC-ITN) "Soft, Small, and Smart: Design, Assembly, and Dynamics of Novel Nanoparticles for Novel Industrial Applications (NanoS3)" (FP7 Grant No. 290251) was also acknowledged. We also thank P&G for financial support *via* the Bristol Final Year Industrial Project Scheme. Synchrotron X-ray access at ESRF CRG XMas beamline and the support by the beamline staff is acknowledged. XMaS is a UK national facility supported by EPSRC.

References

1. Novoselov, K. S., Geim, A. K., Morozov, S. V., Jiang, D., Zhang, Y., Dubonos, S. V., *et al.*, *Electric field effect in atomically thin carbon films.* Science, 2004. **306**(5696): p. 666-669.
2. Novoselov, K. S., Fal'ko, V. I., Colombo, L., Gellert, P. R., Schwab, M. G., and Kim, K., *A roadmap for graphene.* Nature, 2012. **490**(7419): p. 192-200.
3. Geim, A. K., *Graphene: status and prospects.* Science, 2009. **324**(5934): p. 1530-1534.
4. Castro Neto, A. H., Guinea, F., Peres, N. M. R., Novoselov, K. S., and Geim, A. K., *The electronic properties of graphene.* Reviews of Modern Physics, 2009. **81**(1): p. 109-162.
5. Balandin, A. A., *Thermal properties of graphene and nanostructured carbon materials.* Nature Materials, 2011. **10**(8): p. 569-581.
6. Lee, C., Wei, X. D., Kysar, J. W., and Hone, J., *Measurement of the elastic properties and intrinsic strength of monolayer graphene.* Science, 2008. **321**(5887): p. 385-388.
7. Lee, Z., Jeon, K. J., Dato, A., Erni, R., Richardson, T. J., Frenklach, M., *et al.*, *Direct imaging of soft-hard interfaces enabled by graphene.* Nano Letters, 2009. **9**(9): p. 3365-3369.
8. Brownson, D. A. C., Kampouris, D. K., and Banks, C. E., *An overview of graphene in energy production and storage applications.* Journal of Power Sources, 2011. **196**(11): p. 4873-4885.
9. Wu, Q., Xu, Y. X., Yao, Z. Y., Liu, A. R., and Shi, G. Q., *Supercapacitors based on flexible graphene/polyaniline nanofiber composite films.* Acs Nano, 2010. **4**(4): p. 1963-1970.
10. Schwierz, F., *Graphene transistors.* Nature Nanotechnology, 2010. **5**(7): p. 487-496.
11. Britnell, L., Gorbachev, R. V., Jalil, R., Belle, B. D., Schedin, F., Mishchenko, A., *et al.*, *Field-effect tunneling transistor based on vertical graphene heterostructures.* Science, 2012. **335**(6071): p. 947-950.
12. Leenaerts, O., Partoens, B., and Peeters, F. M., *Adsorption of H(2)O, NH(3), CO, NO(2), and NO on graphene: a first-principles study.* Physical Review B, 2008. **77**(12).
13. Melios, C., Giusca, C. E., Panchal, V., and Kazakova, O., *Water on graphene: review of recent progress.* 2d Materials, 2018. **5**(2).
14. Wang, Y., Li, Z. H., Wang, J., Li, J. H., and Lin, Y. H., *Graphene and graphene oxide: biofunctionalization and applications in biotechnology.* Trends in Biotechnology, 2011. **29**(5): p. 205-212.

15. Xu, M. S., Fujita, D., Gao, J. H., and Hanagata, N., *Auger Electron Spectroscopy: A rational method for determining thickness of graphene films.* Acs Nano, 2010. **4**(5): p. 2937-2945.
16. Jang, W. Y., Chen, Z., Bao, W. Z., Lau, C. N., and Dames, C., *Thickness-dependent thermal conductivity of encased graphene and ultrathin graphite.* Nano Letters, 2010. **10**(10): p. 3909-3913.
17. Rutter, G. M., Crain, J. N., Guisinger, N. P., Li, T., First, P. N., and Stroscio, J. A., *Scattering and interference in epitaxial graphene.* Science, 2007. **317**(5835): p. 219-222.
18. Aitken, Z. H. and Huang, R., *Effects of mismatch strain and substrate surface corrugation on morphology of supported monolayer graphene.* Journal of Applied Physics, 2010. **107**(12): p. 10.
19. Robertson, A. W., Allen, C. S., Wu, Y. A., He, K., Olivier, J., Neethling, J., *et al.*, *Spatial control of defect creation in graphene at the nanoscale.* Nature Communications, 2012. **3**.
20. Banhart, F., Kotakoski, J., and Krasheninnikov, A. V., *Structural defects in graphene.* Acs Nano, 2011. **5**(1): p. 26-41.
21. Lin, Y. C., Lu, C. C., Yeh, C. H., Jin, C. H., Suenaga, K., and Chiu, P. W., *Graphene annealing: how clean can it be?* Nano Letters, 2012. **12**(1): p. 414-419.
22. Ni, Z. H., Ponomarenko, L. A., Nair, R. R., Yang, R., Anissimova, S., Grigorieva, I. V., *et al.*, *On resonant scatterers as a factor limiting carrier mobility in graphene.* Nano Letters, 2010. **10**(10): p. 3868-3872.
23. Zhou, H., Ganesh, P., Presser, V., Wander, M. C. F., Fenter, P., Kent, P. R. C., *et al.*, *Understanding controls on interfacial wetting at epitaxial graphene: experiment and theory.* Physical Review B, 2012. **85**(3).
24. Akaishi, A., Yonemaru, T., and Nakamura, J., *Formation of water layers on graphene surfaces.* Acs Omega, 2017. **2**(5): p. 2184-2190.
25. Gurunathan, S. and Kim, J. H., *Synthesis, toxicity, biocompatibility, and biomedical applications of graphene and graphene-related materials.* International Journal of Nanomedicine, 2016. **11**: p. 1927-1945.
26. Lei, H. Z., Zhou, X. J., Wu, H. X., Song, Y., Hu, J., Guo, S. W., *et al.*, *Morphology change and detachment of lipid bilayers from the mica substrate driven by graphene oxide sheets.* Langmuir, 2014. **30**(16): p. 4678-4683.
27. Ang, P. K., Jaiswal, M., Lim, C. H. Y. X., Wang, Y., Sankaran, J., Li, A., *et al.*, *A bioelectronic platform using a graphene-lipid bilayer interface.* Acs Nano, 2010. **4**(12): p. 7387-7394.
28. Frost, R., Jonsson, G. E., Chakarov, D., Svedhem, S., and Kasemo, B., *Graphene oxide and lipid membranes: interactions and nanocomposite structures.* Nano Letters, 2012. **12**(7): p. 3356-3362.
29. Rabti, A., Raouafi, N., and Merkoci, A., *Bio(sensing) devices based on ferrocene-functionalized graphene and carbon nanotubes.* Carbon, 2016. **108**: p. 481-514.
30. Khatayevich, D., Page, T., Gresswell, C., Hayamizu, Y., Grady, W., and Sarikaya, M., *Selective detection of target proteins by peptide-enabled graphene biosensor.* Small, 2014. **10**(8): p. 1505-13, 1504.
31. Briscoe, W. H., Chen, M., Dunlop, I. E., Klein, J., Penfold, J., and Jacobs, R. M. J., *Applying grazing incidence X-ray reflectometry (XRR) to characterising nanofilms on mica.* Journal of Colloid and Interface Science, 2007. **306**(2): p. 459-463.
32. Speranza, F., Pilkington, G. A., Dane, T. G., Cresswell, P. T., Li, P. X., Jacobs, R. M. J., *et al.*, *Quiescent bilayers at the mica-water interface.* Soft Matter, 2013. **9**(29): p. 7028-7041.

33. Sironi, B., Snow, T., Redeker, C., Slastanova, A., Bikondoa, O., Arnold, T., *et al.*, *Structure of lipid multilayers via drop casting of aqueous liposome dispersions.* Soft Matter, 2016. **12**(17): p. 3877-3887.
34. Wlodek, M., Kolasinska-Sojka, M., Wasilewska, M., Bikondoa, O., Briscoe, W. H., and Warszynski, P., *Interfacial and structural characteristics of polyelectrolyte multilayers used as cushions for supported lipid bilayers.* Soft Matter, 2017. **13**(43): p. 7848-7855.
35. Dane, T. G., Cresswell, P. T., Bikondoa, O., Newby, G. E., Arnold, T., Faul, C. F. J., *et al.*, *Structured oligo(aniline) nanofilms via ionic self-assembly.* Soft Matter, 2012. **8**(10): p. 2824-2832.
36. Conrad, M., Rault, J., Utsumi, Y., Garreau, Y., Vlad, A., Coati, A., *et al.*, *Structure and evolution of semiconducting buffer graphene grown on SiC(0001).* Physical Review B, 2017. **96**(19).
37. Emery, J. D., Wheeler, V. H., Johns, J. E., McBriarty, M. E., Detlefs, B., Hersam, M. C., *et al.*, *Structural consequences of hydrogen intercalation of epitaxial graphene on SiC(0001).* Applied Physics Letters, 2014. **105**(16).
38. Zhou, L., Fox, L., Włodek, M., Islas, L., Slastanova, A., Robles, E., *et al.*, *Surface structure of few layer graphene.* Carbon, 2018. **136**: p. 255-261.
39. Ang, P. K., Jaiswal, M., Lim, C., Wang, Y., Sankaran, J., Li, A., *et al.*, *A Bioelectronic Platform Using a Graphene-Lipid Bilayer Interface.* Acs Nano, 2010. **4**(12): p. 7387-7394.
40. Yamazaki, K., Kunii, S., and Ogino, T., *Characterization of interfaces between graphene films and support substrates by observation of lipid membrane formation.* Journal of Physical Chemistry C, 2013. **117**(37): p. 18913-18918.
41. Briscoe, W. H., Speranza, F., Li, P. X., Konovalov, O., Bouchenoire, L., van Stam, J., *et al.*, *Synchrotron XRR study of soft nanofilms at the mica-water interface.* Soft Matter, 2012. **8**(18): p. 5055-5068.
42. Nelson, A., *Co-refinement of multiple-contrast neutron/X-ray reflectivity data using MOTOFIT.* Journal of Applied Crystallography, 2006. **39**: p. 273-276.
43. Porod, G., *Die Röntgenkleinwinkelstreuung von dichtgepackten kolloiden systemen.* Kolloid-Zeitschrift and Zeitschrift Fur Polymere, 1951. **124**(2): p. 83-114.
44. Als-Nielsen, J. and McMorrow, D., *Elements of modern X-ray physics*. 2011, Wiley,: Hoboken. p. xii, 419 pages.
45. Howse, J. R., Steitz, R., Pannek, M., Simon, P., Schubert, D. W., and Findenegg, G. H., *Adsorbed surfactant layers at polymer/liquid interfaces: a neutron reflectivity study.* Physical Chemistry Chemical Physics, 2001. **3**(18): p. 4044-4051.
46. Steitz, R., Gutberlet, T., Hauss, T., Klosgen, B., Krastev, R., Schemmel, S., *et al.*, *Nanobubbles and their precursor layer at the interface of water against a hydrophobic substrate.* Langmuir, 2003. **19**(6): p. 2409-2418.
47. Berkelaar, R. P., Dietrich, E., Kip, G. A. M., Kooij, E. S., Zandvliet, H. J. W., and Lohse, D., *Exposing nanobubble-like objects to a degassed environment.* Soft Matter, 2014. **10**(27): p. 4947-4955.
48. Ashraf, A., Wu, Y. B., Wang, M. C., Aluru, N. R., Dastgheib, S. A., and Nam, S., *Spectroscopic investigation of the wettability of multilayer graphene using highly ordered pyrolytic graphite as a model material.* Langmuir, 2014. **30**(43): p. 12827-12836.
49. Melios, C., Centeno, A., Zurutuza, A., Panchal, V., Giusca, C. E., Spencer, S., *et al.*, *Effects of humidity on the electronic properties of graphene prepared by chemical vapour deposition.* Carbon, 2016. **103**: p. 273-280.

50. Rafiee, J., Mi, X., Gullapalli, H., Thomas, A. V., Yavari, F., Shi, Y. F., *et al.*, *Wetting transparency of graphene.* Nature Materials, 2012. **11**(3): p. 217-222.
51. Ashraf, A., Wu, Y., Wang, M. C., Yong, K., Sun, T., Jing, Y., *et al.*, *Doping-induced tunable wettability and adhesion of graphene.* Nano Lett, 2016. **16**(7): p. 4708-12.
52. Tuteja, A., Choi, W., Ma, M. L., Mabry, J. M., Mazzella, S. A., Rutledge, G. C., *et al.*, *Designing superoleophobic surfaces.* Science, 2007. **318**(5856): p. 1618-1622.
53. Nosonovsky, M. and Bhushan, B., *Superhydrophobic surfaces and emerging applications: non-adhesion, energy, green engineering.* Current Opinion in Colloid & Interface Science, 2009. **14**(4): p. 270-280.
54. Sbragaglia, M., Peters, A. M., Pirat, C., Borkent, B. M., Lammertink, R. G. H., Wessling, M., *et al.*, *Spontaneous breakdown of superhydrophobicity.* Physical Review Letters, 2007. **99**(15).
55. Wehling, T. O., Lichtenstein, A. I., and Katsnelson, M. I., *First-principles studies of water adsorption on graphene: the role of the substrate.* Applied Physics Letters, 2008. **93**(20).
56. Doremus, R. H., *Internal hydroxyl groups near surface of silica.* Journal of Physical Chemistry, 1971. **75**(20): p. 3147-&.
57. Hassanali, A. A. and Singer, S. J., *Model for the water-amorphous silica interface: the undissociated surface.* Journal of Physical Chemistry B, 2007. **111**(38): p. 11181-11193.
58. Sabio, J., Seoanez, C., Fratini, S., Guinea, F., Castro, A. H., and Sols, F., *Electrostatic interactions between graphene layers and their environment.* Physical Review B, 2008. **77**(19).
59. Sun, M. L., Tang, W. C., Ren, Q. Q., Wang, S. K., JinYu, Du, Y. H., *et al.*, *First-principles study of the alkali earth metal atoms adsorption on graphene.* Applied Surface Science, 2015. **356**: p. 668-673.
60. Bostwick, A., Ohta, T., Seyller, T., Horn, K., and Rotenberg, E., *Quasiparticle dynamics in graphene.* Nature Physics, 2007. **3**(1): p. 36-40.
61. Malyi, O. I., Sopiha, K., Kulish, V. V., Tan, T. L., Manzhos, S., and Persson, C., *A computational study of Na behavior on graphene.* Applied Surface Science, 2015. **333**: p. 235-243.
62. McCaffrey, D. L., Nguyen, S. C., Cox, S. J., Weller, H., Alivisatos, A. P., Geissler, P. L., *et al.*, *Mechanism of ion adsorption to aqueous interfaces: graphene/water vs. air/water.* Proceedings of the National Academy of Sciences of the United States of America, 2017. **114**(51): p. 13369-13373.
63. Shi, G. S., Ding, Y. H., and Fang, H. P., *Unexpectedly strong anion-p interactions on the graphene flakes.* Journal of Computational Chemistry, 2012. **33**(14): p. 1328-1337.
64. Tabrizchi, M. and Rouholahnejad, F., *Comparing the effect of pressure and temperature on ion mobilities.* Journal of Physics D-Applied Physics, 2005. **38**(6): p. 857-862.